A Method to Study the Effect of Renewable Resource Variability on Power System Dynamics

Yu Christine Chen, *Student Member, IEEE*, and Alejandro D. Domínguez-García, *Member, IEEE*

***Abstract*—This paper proposes a set-theoretic method to assess the effect of variability associated with renewable-based electricity generation on power system dynamics, with a focus on time-scales involving electromechanical phenomena. Performance requirements define a set within which the values of certain system variables, e.g., synchronous generator speeds, system frequency, or bus voltages, must remain at all times. To address this problem, reachability analysis techniques are used; for a given timeframe, if the reach set, i.e., the set that contains all possible system trajectories, is within the set defined by performance requirements, then it may be concluded that variability arising from in renewable-based electricity generation does not have a significant impact on system dynamics. The proposed method is illustrated through several case studies, including the 39-bus New England system model.**

I. Introduction

The motivation for this work lies in the current trend toward more environmentally friendly electricity generation, which requires increased reliance on renewable resources, such as wind or solar. It is well known that the integration of these renewable-based electricity sources into a power system presents notable challenges in its operation due to the variable nature of wind speed and solar insolation. This introduces uncertainty on the generation side, which affects system operation across different time-scales: day-ahead, hour-ahead, and five-minute-ahead scheduling; automatic generation control, and governor response [1]. The focus of this work is on the impact of variability in renewable-based generation on power system dynamic performance, particularly, on time-scales involving electromechanical phenomena [2], with time-frames of interest of up to 100 s. On these scales, deep levels of wind penetration may impact small-signal and transient stability due to reduction of system effective inertia [3], and primary frequency control due to displacement of units providing governor response [4].

Various approaches to address uncertainty in power systems have been explored in the context of both power flow analysis and dynamic performance assessment. These approaches include probabilistic and set-theoretic (unknown-but-bounded) uncertainty characterizations. In this paper, we pursue the unknown-but-bounded approach, building on previous results reported in [5]. Previous work that used set-theoretic uncertainty characterizations mainly focused on static analysis. For example, the authors in [6] use interval arithmetics to capture uncertainty in power flow computations. The effect of model parameter uncertainty on transmission security in a power market is explored in [7]. Interval analysis, in conjunction with a linearized power system model, is used to determine the worst-case effects of network parameter uncertainties on various optimization problems solved in a deregulated power market [8]. Furthermore, [9] uses ellipsoidal approximations in power system optimization to obtain ranges in which generator injections can vary without violating operational constraints in static security analysis. In dynamic performance analysis, the authors in [10], [11] use sensitivity analysis techniques to generate accurate first-order approximations of trajectories that arise from perturbed parameter sets. The work in [12], [13] uses backward reach sets to compute the stability region of an equilibrium point.

In this paper, we develop an analytically tractable method to assess whether in a particular timeframe, certain state variables of interest remain within acceptable ranges for all possible realizations of renewable-based electric power generation that arise from variability in their primary energy source. In this regard, the method can be used to verify the performance of power system closed-loop controls, which are responsible for maintaining acceptable performance, for different scenarios of wind penetration. This type of verification analysis is a common step in control system performance analysis when the system dynamics is perturbed by an uncertain input disturbance.

In the context of this paper, the power injected by renewable resources can be described (under certain simplifying assumptions described in Section II) as an uncertain disturbance to the system dynamics. Specifically, for a given timeframe, the amount of renewable-based generation can be described by some nominal generation profile (given by a forecast) and some confidence interval around each point of this generation profile (e.g., forecast error). As mentioned above, an application of the tool is to verify whether power system closed-loop controls can handle this uncertainty by ensuring that performance requirements are met, and also ruling out undesired behaviors such as the ones described in [11].

One way to address the verification problem described above is to repeatedly simulate the system dynamic behavior for many different (renewable-based) generation profiles (described as functions of time). Alternatively, the problem can be addressed by computing the system reach set [14], i.e., the set that bounds all possible system trajectories that arise from all possible renewable-based power generation profiles. Computing the exact reach set of a nonlinear differential-algebraic

The authors are with the Department of Electrical and Computer Engineering of the University of Illinois at Urbana-Champaign. E-mail: {chen267, aledan}@illinois.edu.

Work supported by the National Science Foundation under grant ECCS-0925754 and by the Natural Sciences and Engineering Research Council of Canada under its Postgraduate Scholarship Program.

equations (DAEs) may be very difficult, or even impossible. For the timeframes of interest (up to 100 s), it is assumed that the disturbance to the system dynamics introduced by (uncertain) variations around the nominal generation profile is sufficiently small. This justifies approximating the DAE reach set by that of a dynamical model that results from linearizing the DAE around the trajectory that arises from the renewable-based nominal generation profile.

We now discuss our method's role in the hierarchy of power system dynamic performance analysis. On one hand, in small-signal stability analysis, the canonical problem is to study the stability of power system equilibrium points through eigenvalue analysis (see [2], [15]). On the other hand, transient stability is used to study the time-evolution of a power system trajectory when subject to a large perturbation, e.g., a fault in a transmission line (see [2], [15]). We believe that our tool complements these two types of analysis as it attempts to characterize the effect of *time-evolving* perturbations that originate from the (uncertain) variability of renewable-based electricity generation on power system dynamics. More precisely, it can be considered as belonging to a class of tools for power system trajectory sensitivity analysis (see e.g., [10], [11]).

Application of the proposed method is illustrated through two case studies. The first one involves a three-bus system, the size of which enables us to derive explicit expressions in all steps involved in the analysis. The second one involves the 39-bus New England system model, where the impact of wind on power system dynamics for 20% and 30% penetration is studied, with different synchronous generator displacement scenarios, different wind variability levels, and different units participating in governor response.

The remainder of this paper is organized as follows. Section II presents the modeling framework. Section III describes the proposed dynamic performance assessment method. Sections IV and V illustrate the assessment method with a three-bus and a 39-bus system example respectively. Concluding remarks are made in Section VI.

II. Modeling Framework

In this section, we present the modeling framework, which includes the canonical power system DAE model, the renewable-based electricity source model, and the augmented DAE model that results from accounting for the dynamics of renewable-based electricity sources. The model describing the primary energy source variability is also introduced.

A. Renewable-Based Electricity Resource Model

It is assumed that under normal system operating conditions (no faults in the network or sudden loss of synchronous generators) and for the time-scales of interest, the interaction between a renewable-based electricity source and the network is predominantly through its power injection. This injection can be described by a dynamical model that relates the renewable-based source power output to its primary energy source. For wind turbine generators, this assumption is consistent with the findings in [16], where it is shown through model order reduction that a low-order dynamical model yields a simple yet accurate description of the relation between wind speed and power generated by a Type-C wind turbine.

Following the ideas above, we assume that a wind power plant can be represented by a dynamical model that includes all individual wind turbine generators, where the power injection in the grid is a function of wind speeds at points where wind turbines are located. Following [17] (also [18, ch. 2]), this model can be further reduced by aggregating individual wind turbine generator models, which results in the power injection being a function of a single wind speed representative of the plant location. Letting $w_i(t) \in \mathbb{R}$ denote the representative wind speed (or insolation) for the i^{th} wind (or solar) power plant at time t, the power injection arising from the renewable plant can then be described by

$$\begin{aligned} \dot{z}_i &= \alpha_i(z_i, w_i), \\ P_i &= \beta_i(z_i), \end{aligned} \tag{1}$$

where $z_i \in \mathbb{R}^{n_i}$, $P_i(t)$ is the output power, $\alpha_i : \mathbb{R}^{n_i+1} \mapsto \mathbb{R}^{n_i}$, and $\beta_i : \mathbb{R}^{n_i} \mapsto \mathbb{R}^+$.

B. System DAE Model

In order to describe the electromechanical behavior of the power system, the standard DAE model is formulated to explicitly account for renewable-resource dynamics using the model in (1). Assume the system contains r buses with power injections arising from renewable resources or aggregations thereof. Then, following the notation in (1), define $z = [z_1^T, \ldots, z_r^T]^T$, $w = [w_1, \ldots, w_r]^T$, and the vector functions $\alpha(z, w) = [\alpha_1^T(z_1, w_1), \ldots, \alpha_r^T(z_r, w_r)]^T$ and $\beta(z) = [\beta_1(z_1), \ldots, \beta_r(z_r)]^T$. Also, define $v = [P_1, \ldots, P_r]^T$, where each P_i is the power output of renewable resource i as described in (1), from where it follows that $v = \beta(z)$. Then the system electromechanical behavior can be described by a DAE model of the form

$$\begin{aligned} \dot{x} &= g(x, y, u), \\ \dot{z} &= \alpha(z, w), \\ v &= \beta(z), \\ 0 &= h(x, y, v), \end{aligned} \tag{2}$$

with $g : \mathbb{R}^{n+p+m} \mapsto \mathbb{R}^n$, $h : \mathbb{R}^{n+p+l} \mapsto \mathbb{R}^p$, and where $x \in \mathbb{R}^n$ includes the synchronous machine dynamic states, $y \in \mathbb{R}^p$ includes the bus voltage magnitudes and angles, and $u \in \mathbb{R}^m$ includes the synchronous machine set points. In (2), we assume that the rotor angle of a particular synchronous generator provides the reference and all other rotor angles and bus voltages are defined relative to this reference [2].

The model in (2) is similar to the standard electromechanical models in the literature (see e.g., [2], [15]) except for the way in which the power injections from renewable-energy resources are modeled. In particular, in the general device power injection model described in [15, §9.1], the state vector for each device contains *external* variables shared with other devices. In our case, due to the assumptions for reducing the order of the renewable-based electricity source model described in (2) by $\dot{z} = \alpha(z, w)$, the model does not share external variables with the conventional dynamic model for the conventional generators described in (2) by $\dot{x} = g(x, y, u)$.

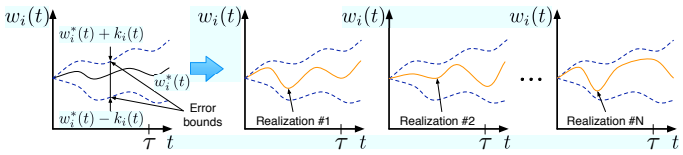

Fig. 1: Renewable-based power injection model.

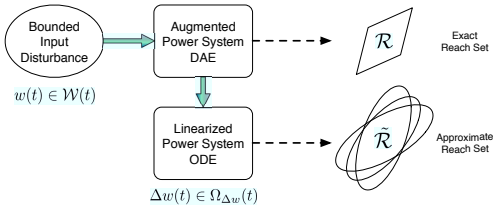

Fig. 2: Dynamic performance assessment framework.

While, this difference is perhaps not substantial, it allows us to have an aggregate reduced-order model for the renewable-based resources that substantially decreases the dimension of the state space. Additionally, for solar photovoltaic installations, the maximum power point tracker sets power output as a function of insolation. With respect to the time-scales of interest here, and given that there are no moving parts, it can be assumed that power output changes instantaneously with changes in insolation, i.e., the relation between power output and insolation is algebraic. Such a static insolation/output-power model is consistent with the models in [19], and can be easily recovered from the more general dynamical model $\dot{z} = \alpha(z, w)$ by setting $\dot{z} = 0$.

C. Primary Energy Source Variability Model

Variability in the primary energy sources of a renewable-based electricity source is modeled as an unknown-but-bounded quantity. For example, wind speed or solar insolation are assumed to lie within some interval around a nominal value, which could result from forecast or could be chosen based on engineering judgment. The model, which captures all possible primary energy source realizations as time evolves, is graphically depicted in Fig. 1.

Let $w_i^*(t)$ denote the nominal value of wind speed (or insolation) at time t for renewable resource i. Additionally, the (unknown) actual value of wind speed (or insolation) at time t, which is denoted by $w_i(t)$, is assumed to lie within some interval around the nominal $w_i^*(t)$ value. Then the variability in $w_i(t) \in \mathbb{R}$ can be described by

$$w_i(t) \in \mathcal{W}_i(t) = \{w_i(t) : \ |w_i(t) - w_i^*(t)| \leq k_i(t)\}. \quad (3)$$

Accounting for all r renewable-based electricity sources in the system, it follows that

$$w(t) \in \mathcal{W}(t) = \mathcal{W}_1(t) \times \cdots \times \mathcal{W}_r(t) \subseteq \mathbb{R}^r. \quad (4)$$

Equivalently, wind speed (or insolation) can be expressed as $w_i(t) = w_i^*(t) + \Delta w_i(t)$, where $\Delta w_i(t) \in \mathbb{R}$ is given by

$$\Delta w_i(t) \in \Delta\mathcal{W}_i(t) = \{\Delta w_i(t) : \ |\Delta w_i(t)| \leq k_i(t)\}, \quad (5)$$

and

$$\Delta w(t) \in \Delta\mathcal{W}(t) = \Delta\mathcal{W}_1(t) \times \cdots \times \Delta\mathcal{W}_r(t) \subseteq \mathbb{R}^r. \quad (6)$$

III. Dynamic Performance Assessment

In this section, we develop a method to assess the dynamic performance for all feasible realizations of renewable-based power generation that arise from primary energy source variability. In this method, the DAE model is linearized along a nominal trajectory that results from some nominal renewable-based generation. Assuming primary energy source variability is sufficiently small, the linearized model is used to approximate the DAE reach set, which contains all trajectories arising from all possible primary energy source realizations. The reach set can be used to assess whether certain state variables remain within a region of the state space defined by performance requirements at all times. The method is summarized in Fig. 2, and formalized next.

A. Linearized Model

Let τ denote the timeframe of interest (up to 100 s). Then, for $0 \leq t \leq \tau$, assuming the augmented DAE system in (2) evolves from $x(0) = x_0$, $y(0) = y_0$, and $z(0) = z_0$ according to nominal set points $u(t) = u^*(t)$ and wind speed (or insolation) $w(t) = w^*(t)$, a nominal trajectory, described by the 3-tuple, (x^*, y^*, z^*), results. Assume that the functions $g(\cdot)$, $\alpha(\cdot)$, $\beta(\cdot)$, and $h(\cdot)$ in (2) are continuously differentiable with respect to their arguments in some neighborhood of $\big(x^*(t), y^*(t), z^*(t), u^*(t), w^*(t)\big)$, $0 \leq t \leq \tau$. Let $x(t) = x^*(t) + \Delta x(t)$, $y(t) = y^*(t) + \Delta y(t)$, $z(t) = z^*(t) + \Delta z(t)$, where $\Delta x(t)$, $\Delta y(t)$, and $\Delta z(t)$ result from $\Delta w(t) = w(t) - w^*(t)$. We assume that along the nominal trajectory (x^*, y^*, z^*), invertibility of the power flow equations' Jacobian always holds. Then, assuming $\Delta w(t) \in \Delta\mathcal{W}(t)$ is sufficiently small, using a variational approach [20], we can obtain a linear, time-varying ordinary differential equation (ODE) model of the form:

$$\frac{d}{dt}\Delta\tilde{x} = A(t)\Delta\tilde{x} + B(t)\Delta w, \quad (7)$$

where $\Delta\tilde{x} = [\Delta x^T, \Delta z^T]^T$, and $\Delta\tilde{x}(0) = 0$. The derivation of $A(t)$ and $B(t)$ is provided in Appendix A.

B. Reachability Analysis

The objective is to obtain the reach set of the augmented DAE model in (2), which is the set that contains all trajectories that arise from all feasible values of the primary source of energy $w(t) \in \mathcal{W}(t)$, for $0 \leq t \leq \tau$. Computing the exact shape of the reach set $\mathcal{R}(t)$ can be very difficult, or even impossible, especially for nonlinear DAEs. Thus, instead of computing $\mathcal{R}(t)$, for $0 \leq t \leq \tau$, we assume that the disturbance $\Delta w(t)$ is sufficiently small to justify the approximation of the DAE reach set by that of the linearized model in (7). Thus, we obtain an upper bound to the reach set of (7), which we denote by $\Delta\mathcal{R}(t)$, and assume that $\mathcal{R}(t) \approx x^*(t) \oplus \Delta\mathcal{R}(t) =: \tilde{\mathcal{R}}(t)$, where $\oplus$ denotes the Minkovski sum. Also, since the reach set of the linearized system in (7) is only an approximation to that of the nonlinear system in (2), it suffices to obtain an upper bound instead of calculating the exact reach set of (7).

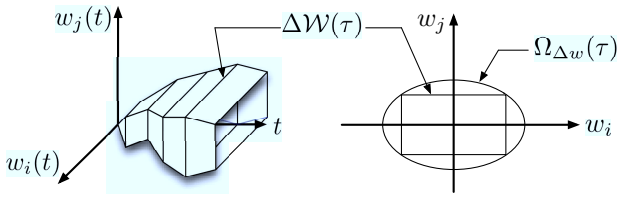

Fig. 3: Input set $\Delta\mathcal{W}(t)$ and its ellipsoidal bound $\Omega_{\Delta w}(t)$.

Although there exists several different methods for linear-ODE reachability analysis, we use ellipsoidal-based techniques, which have a long history in control theory (see e.g., [14], [21], [22], [23], and the references therein). We introduce next the fundamental ideas for reachability analysis using ellipsoidal techniques, and illustrate them with several examples. Then, we provide a formal comparison, in terms of computational complexity, of ellipsoidal techniques against other techniques for reachability analysis of ODEs.

1) Computing the input set ellipsoidal bound: In ellipsoidal-based reachability analysis, as depicted in Fig. 3, at every time instant t, the input set $\Delta\mathcal{W}(t)$ is bounded by an ellipsoid $\Omega_{\Delta w}(t)$, i.e., $\Delta\mathcal{W}(t) \subseteq \Omega_{\Delta w}(t)$, defined as

$$\Omega_{\Delta w}(t) := \left\{\Delta w(t) : \Delta w^T(t) Q^{-1}(t) \Delta w(t) \leq 1\right\}, \quad (8)$$

where $Q(t)$ is a positive definite shape matrix. Thus, for every t, given $\Delta\mathcal{W}(t)$, it is necessary to obtain an upper bound $\Omega_{\Delta w}(t)$ that is optimal in some sense. For example, a choice for $Q(t)$ is one that minimizes the volume of the resulting bounding ellipsoid $\Omega_{\Delta w}(t)$. Since the volume of $\Omega_{\Delta w}(t)$ is proportional to $(\det Q(t))^{1/2}$ [24], computing the shape matrix $Q(t)$ that minimizes the volume of $\Omega_{\Delta w}(t)$ and contains $\Delta\mathcal{W}(t)$ can be formulated as the following convex optimization problem [25]:

$$\begin{aligned} &\text{minimize} && (\det Q(t))^{1/2} \\ &\text{subject to} && v^T Q^{-1}(t) v \leq 1, \quad \forall v \in \Delta\mathcal{W}. \end{aligned} \quad (9)$$

Other criteria to choose $Q(t),\ \forall t$, includes minimizing the span of $\Omega_{\Delta w}(t)$ on a particular direction defined by a vector $\rho \in \mathcal{R}^r$, which results in an optimization problem where the objective is to minimize the support function of $\Omega_{\Delta w}(t)$ for ρ. In the case studies presented in Sections IV and V, we use the minimum volume criterion.

Remark 1: Although in theory it is necessary to obtain $Q(t)$ for every $t \in [0, \tau)$, in practice, it is only calculated at discrete time instants $t_0, t_1, \ldots, t_i, t_{i+1}, \ldots, \tau$, and in the interval between two time instants $[t_i, t_{i+1})$, $Q(t_i)$ is used only to be updated to $Q(t_{i+1})$ at t_{i+1}. An alternative to updating $Q(t)$ at discrete time instants is to use a fixed Q, which corresponds to the shape matrix of an ellipsoid $\mathcal{E}$ such that $\Omega_{\Delta w}(t) \subseteq \mathcal{E}$, for $0 \leq t \leq \tau$. This results in a conservative upper-bound on the calculation of $\mathcal{R}(t)$, but substantially speeds up the analysis. ■

2) Propagating the input set ellipsoidal bound: Once the input set bounding ellipsoid $\Omega_{\Delta w}(t)$ is obtained, it can be propagated through the system dynamics to obtain a family of ellipsoids $\mathcal{X}(t) = \{\mathcal{X}_\beta(t),\ \beta > 0\}$, the members of which provide upper bounds on the exact reach set $\Delta\mathcal{R}(t)$ of (7). Each ellipsoid $\mathcal{X}_\beta(t)$ in $\mathcal{X}(t)$ is defined as

$$\mathcal{X}_\beta(t) = \{x : x^T \Psi_\beta^{-1}(t) x \leq 1\}, \quad (10)$$

where Ψ_β is a positive definite shape matrix obtained as

$$\begin{aligned} \frac{d}{dt}\Psi_\beta(t) =& A(t)\Psi_\beta(t) + \Psi_\beta(t)A^T(t) + \\ & \beta\Psi_\beta(t) + \frac{1}{\beta} B(t)Q(t)B^T(t), \end{aligned} \quad (11)$$

with $\Psi(0) = \Psi_0$. The exact reach set $\Delta\mathcal{R}(t)$ (evaluated for a time instant t) of the small-signal model (7) can be upper bounded by the intersection of the ellipsoids in the family $\mathcal{X}(t)$:

$$\Delta\mathcal{R}(t) \subseteq \bigcap_\beta \mathcal{X}_\beta(t),\ \forall\ \beta \in \mathbb{R} \text{ such that } \beta > 0. \quad (12)$$

Then, the set $\Delta\mathcal{R}$ containing all possible Δx trajectory approximations, for $0 \leq t \leq \tau$, is given by

$$\Delta\mathcal{R} = \bigcup_{t=0}^{\tau} \Delta\mathcal{R}(t). \quad (13)$$

The result in (11) can be obtained through set calculations [14], or derived from Pontryagin's maximum principle [23]. The parameter $\beta > 0$ (possibly time-varying) is arbitrary and determines the shape of the bounding ellipsoids. We next discuss a few alternatives for choosing β.

3) Choice of Parameter β: From (12), it is obvious that in order to obtain an upper bound on $\Delta\mathcal{R}(t)$, it suffices to obtain a single $\mathcal{X}_\beta(t)$ for some $\beta > 0$. In this regard, we may be interested in obtaining a bounding ellipsoid that is optimal in some sense. For example, an alternative is to choose a single β that minimizes the volume of the resulting bounding ellipsoid $\mathcal{X}_\beta(t)$ is minimum for all $t > 0$ [22]. This can be achieved by choosing a time-varying $\beta(t)$ of the form

$$\beta(t) = \sqrt{\frac{\text{tr}(\Psi_\beta^{-1}(t)B(t)Q(t)B(t)^T)}{n}}, \quad (14)$$

where $\text{tr}(\Psi_\beta^{-1}(t)BQB^T)$ denotes the trace of $\Psi_\beta^{-1}(t)BQB^T$. However, with this choice of $\beta(t)$, the matrix differential equation in (11) becomes nonlinear, posing some additional challenges in terms of obtaining its solution numerically.

The accuracy of the approximation can be substantially increased by obtaining more than one bounding ellipsoid, and it is even possible to obtain the exact reach set in some cases. For example, if the system in (7) were controllable[1], the authors in [23] showed that choosing $\beta(t)$'s of the form

$$\beta(t) = \sqrt{\frac{\eta^T e^{At} B(t)Q(t)B^T(t)e^{A^T t}\eta}{\eta'\Psi_\eta(t)\eta}}, \quad (15)$$

for all $\eta \in \mathbb{R}^n$ such that $\eta'\eta = 1$, results in a family of bounding ellipsoids such that $\Delta\mathcal{R}(t) = \bigcap_\beta \mathcal{X}_\beta(t)$, i.e., the intersection of the family of ellipsoids generated with (11) and (15) yields the exact reach set. While this approach for choosing β is appealing in theory, in practice, it is not possible

[1]A linear system $\frac{dx}{dt} = Ax + Bu$, with $x \in \mathbb{R}^n$ is controllable if and only if the controllability matrix $\mathcal{C} = \begin{bmatrix} B & AB & A^2B & \ldots & A^{n-1}B \end{bmatrix}$ is full rank.

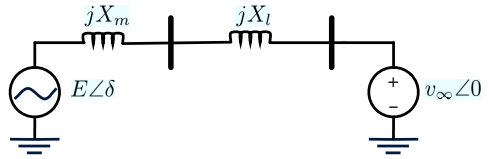

Fig. 4: Single-machine infinite bus system.

to compute $\mathcal{X}_\beta(t)$ for infinitely many values of β (although accurate approximations can be obtained by using a few η's appropriately chosen). Additionally, the matrix differential equation in (11) becomes nonlinear, posing computational challenges. For uncontrollable systems, we can only choose η's in the image of the controllability matrix (otherwise, $\beta(t) = 0$, $\forall t$, and the matrix differential equation in (11) is not properly defined).

A practical alternative adopted in this work to circumvent the problems described above with the particular choice of β in (14) and (15) is to randomly choose several positive and constant values of β, which makes the matrix differential equation in (11) linear and simplifies its numerical solution by allowing it to be rewritten as a set of differential equations as follows. Let $X \otimes Y$ denote the Kronecker product of matrices X and Y (see, e.g., [26]). Denote by $\psi_\beta \in \mathbb{R}^{n^2}$ the vector that results from stacking up the columns of the matrix $\Psi_b \in \mathbb{R}^{n\times n}$, and by $b \in \mathbb{R}^n$ the vector that results from stacking up the columns of the matrix $B\tilde{Q}B \in \mathbb{R}^{n^2}$. Then,

$$\frac{d}{dt}\psi_\beta = \tilde{A}\psi_\beta + b, \tag{16}$$

with $\tilde{A} = I_n \otimes A + A \otimes I_n + \beta I_{n^2}$, where I_n and I_{n^2} denote the $n \times n$ and the $n^2 \times n^2$ identity matrices, respectively.

Remark 2: It is important to note that although the size of (16) is n^2, in practice, since Ψ_β is a symmetric matrix, it is possible to reduce the size of (16) to $n(n+1)/2$. Also, it is possible to numerically solve in parallel all these systems using, e.g., the MATLAB parallel toolbox, although for each β, a different system of differential equations results. We used these ideas in the code we developed to analyze the case-studies presented in Sections IV and V. ■

We illustrate the application of the reachability concepts introduced above with the following example featuring the single-machine infinite-bus (SMIB) system. Since the purpose of this example is to illustrate notions, without loss of generality, we restrict the analysis to the case when the infinite bus voltage magnitude is uncertain.

Example 1: Consider the SMIB system in Fig. 4, where the synchronous generator is described by the classical model. Assume that the infinite bus voltage magnitude v_∞ can vary over time; however, the time structure of this variation is not known except for upper and lower bounds, i.e., v_∞ is unknown but bounded. Let the maximum and minimum values of the variation be ± 0.1 pu around a nominal value of $v_m = 1$ pu, i.e., $v_\infty \in [0.9, 1.1]$ pu, from where it follows that $|\Delta v_\infty| < 0.1$, or $\Delta v_\infty^2 < 0.01$. Therefore, following the notation in (8), this results in $Q(t) = 0.01$, $0 \le t \le \tau$. In this particular case, since v_m is a constant, the system that results from linearizing the SMIB model will be time invariant.

TABLE I: SMIB System Model Parameter Values

E	X_m	X_l	M	D [s/rad]	T_m	ω_s [rad/s]	v_m
1	0.2	0.066	$\frac{1}{15\pi}$	0.08	1	120π	1

Let δ be the angular position of the rotor in electrical radians, and ω be the angular velocity of the rotor in electrical rad/s. Define $\Delta\delta = \delta - \delta_0$, $\Delta\omega = \omega - \omega_0$, and $\Delta v_\infty = v_\infty - v_m$. Then, by linearizing the SMIB model, we obtain

$$\frac{d}{dt}\begin{bmatrix}\Delta\delta\\ \Delta\omega\end{bmatrix} = \begin{bmatrix} 0 & 1 \\ -\frac{Ev_m}{M(X_m+X_l)}\cos\delta_0 & -\frac{D}{M}\end{bmatrix}\begin{bmatrix}\Delta\delta\\ \Delta\omega\end{bmatrix} + \begin{bmatrix}0\\ -\frac{T_m}{Mv_m}\end{bmatrix}\Delta v_\infty, \tag{17}$$

where D, M, E, X_m, X_l, ω_s, and T_m are constants [2].

Reachability analysis is conducted for $\tau = 20$ s using the values given in Table I. We assume that the initial conditions are known: $[\Delta\delta(0), \Delta\omega(0)]^T = [0,0]^T$, $\Psi_0 \in \mathbb{R}^{2\times 2}$ is a zero matrix. In Fig. 5(a), we plot the minimum volume ellipsoid, $\mathcal{X}_0$, which results from solving (11) with β defined in (14). In the same figure, by solving (11) with β defined in (15) for $\eta = [0,1]^T =: \eta_1$, $\eta = [0.9962, 0.0872]^T =: \eta_2$, and $\eta = [-0.9986, 0.0523]^T =: \eta_3$, we obtain three ellipsoids $\mathcal{X}_{\eta_1}$, $\mathcal{X}_{\eta_2}$, $\mathcal{X}_{\eta_3}$ (all of which bound the reach set of the system in (17) and thus so does their intersection). Additionally, a worst-case system trajectory obtained by simulating the nonlinear SMIB model is plotted in Fig. 5(a). This worst-case trajectory is obtained by switching the value of v_∞ between 0.9 (its minimum) and 1.1 (its maximum). This worst-case trajectory and minimum volume ellipsoidal reach set are reproduced in Fig. 5(b). Additionally, Fig. 5(b) also contains three bounding ellipsoids $\mathcal{X}_{\beta_1}$, $\mathcal{X}_{\beta_2}$, $\mathcal{X}_{\beta_3}$ corresponding to three randomly chosen constant β's: $\beta = 0.64 =: \beta_1$, $\beta = 0.74 =: \beta_2$, and $\beta = 0.84 =: \beta_3$, respectively. From both Figs. 5(a) and 5(b), we see that the linearized small-signal reach set fully contains the system state excursions of the nonlinear system, providing a fairly accurate approximation to the nonlinear model reach set. ■

4) Alternative methods for reachabiltiy analysis: Other methods for reachability analysis of ODEs include the use of regular polytopes [27], and symmetric polytopes [28]. Although regular polytopes can provide tight approximations for any convex set, the complexity of numerical algorithms that use polytopes for reachability analysis is V^n, where V is the number of vertices of the polytope and n is the dimension of the state space [11], [29]. Symmetric polytopes (or zonotopes) have been proposed as an alternative to polytopes and ellipsoids as they are closed under the Minkovski sum; however as time increases, the order of bounding zonotope increases by a factor equal to the order of the zonotope describing the initial conditions divided by n. On the other hand, ellipsoidal-based reachability algorithms grow in complexity as $O(n^3)$ with the dimension of the state space, and linearly with the number of time steps and the number of bounding ellipsoids [29]. The reader is referred to [30] for further discussion and comparison between different techniques for reachability analysis.

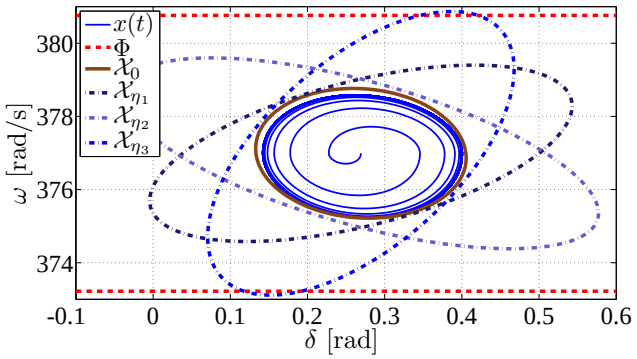

(a) Worst-case trajectory compared to minimum volume ellipsoid and three ellipsoids with βs obtained from (15).

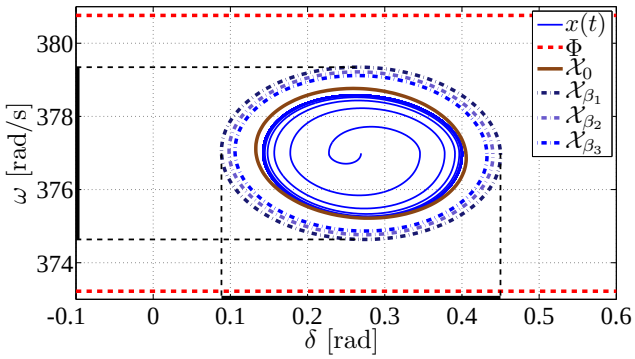

(b) Worst-case trajectory compared to minimum volume ellipsoid and three ellipsoids with randomly chosen βs.

Fig. 5: SMIB system reachability analysis results for infinite bus voltage variation of ± 0.1 pu.

C. Performance Requirements Verification

Performance requirements generally consist of constraints in the form of interval ranges on variables of interest such as system frequency and synchronous generator speeds. In general, performance requirements constrain the excursions of $x(t)$ around some $x_0(t) \in \mathbb{R}^n$ to a region of the state space $\Phi \subseteq \mathbb{R}^n$ defined by a symmetric polytope:

$$\Phi(t) = \{x(t) : |\pi_i^T \big(x(t) - x_0(t)\big)| \leq 1, \forall i = 1, 2, \ldots, p\}, \tag{18}$$

where $\pi_i \in \mathbb{R}^n$. The computation of the reach set allows us to determine whether the performance requirements are violated. In fact, verifying that the system meets all performance requirements for any $w(t) \in \mathcal{W}(t)$, is equivalent to checking that $\mathcal{R}(t) \subseteq \Phi(t)$, for $0 \leq t \leq \tau$. As explained in Section III-B, we assume that $\mathcal{R}(t) \approx \tilde{\mathcal{R}}(t)$ for $0 \leq t \leq \tau$; then, instead of checking that $\mathcal{R}(t) \subseteq \Phi(t)$, we check that $\tilde{\mathcal{R}}(t) \subseteq \Phi(t)$.

The ideas above are illustrated in the following example, which is a continuation of Example 1.

Example 2: Consider the SMIB discussed in Example 1. Assume that the synchronous generator is equipped with an under-speed protection that causes it to disconnect below 373.2 rad/s (59.4 Hz) and an over-speed protection that also disconnects the generator above 380.6 rad/s (60.6 Hz). In this case, and following the notation in (18), $\pi_1 = [0, \frac{1}{1.2\pi}]^T$. Therefore the performance requirements set is defined as

$$\Phi(t) = \{\omega(t) : |\omega(t) - \omega_s| \leq 1.2\pi\}, \tag{19}$$

where $\omega_s = 120\pi$ rad/s. In Fig. 5, the performance requirements set described by (19) corresponds to the two horizontal dashed lines. It is easy to check by visual inspection that the intersection of the ellipsoids in Fig 5(a), as well as all the ellipsoids in Fig 5(a) are fully contained within the region defined by the two horizontal dashed lines. Then, we conclude that despite the variability in the infinite bus voltage magnitude, the speed protection on the generator will not cause it to inadvertently disconnect. ■

D. Results Visualization

Visualization of the ellipsoids in Example 1, and thus checking whether or not $\tilde{\mathcal{R}}(t) \subseteq \Phi(t)$ is satisfied, is straightforward since the two state variables can be plotted directly onto the Cartesian plane. Even for the case when there are three state variables, we can still plot the resulting three-dimensional ellipsoids. In general, systems with $q > 3$ states result in q-dimensional ellipsoids. To assess whether a state variable of interest, denoted as $\Delta\tilde{x}_i$ [i.e., the i^{th} component of $\Delta\tilde{x} \in \mathbb{R}^q$ in (7)], lies within acceptable ranges, we project the corresponding q-dimensional ellipsoid $\mathcal{X}$ onto a subspace spanned by the ith axis of $\Delta\tilde{x}$.

Define the projector H_i to be a $1 \times q$ matrix with all entries equal to zero except for the i^{th} one, which is set to one. Then, the projection of $\mathcal{X}(t)$ onto the subspace spanned by the i^{th} axis of the i^{th} dimension is

$$d\Pi_i(\mathcal{X}) = \{\Delta x_i : \Delta x_i^T (H\Psi H^T)^{-1}(t)\Delta x_i \leq 1\}. \tag{20}$$

It is also possible to plot the projection of $\mathcal{X}(t)$ onto the subspace spanned by the i^{th} and j^{th} axis, corresponding to $\Delta\tilde{x}_i$ and $\Delta\tilde{x}_j$ dimensions, by defining the projector H_{ij} to be a $2 \times q$ matrix will all entries equal to zero except the $(1, i)$ and the $(2, j)$ entries, which are set to one. We illustrate these ideas in the following example and use them in the case studies of Sections IV–V.

Example 3: Consider, again, the SMIB system of Examples 1 and 2. Even though the system has only two state variables and can be plotted in a straightforward manner onto the Cartesian plane, we may be interested in only the behavior of one of the variables and wish to obtain its maximum deviations around an operating point. To obtain the projection onto δ, we choose the projector $H_1 = [1, 0]$ and, similarly for ω, $H_2 = [0, 1]$. A geometric interpretation is shown in Fig. 5(b), where the outermost ellipsoid is projected onto both the δ and ω axes via the thin dashed lines and the corresponding projections are plotted in thick lines on the axes. Again, we conclude ω deviations are completely contained within the interval between 59.4 Hz and 60.6 Hz. ■

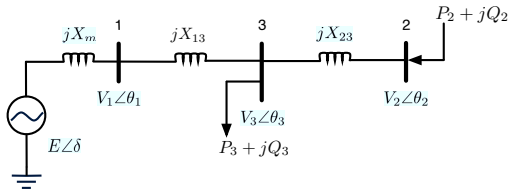

Fig. 6: Three-bus system with a wind turbine generator.

IV. Three-Bus System Case Study

In this section, we use the methodology described in the previous section to analyze a three-bus power system depicted in Fig. 6, consisting of a synchronous generator connected to Bus 1, a renewable-based generating resource connected to bus 2, and a load connected to Bus 3. The electrical network is assumed to be lossless and is described by the standard power flow equations. We will analyze this system for different synchronous generator and wind turbine generator (WTG) models. Unless otherwise stated, all quantities are in per unit (pu). As in Example 2, the performance criteria adopted is the synchronous machine speed excursion—a surrogate for system frequency [2].

A. Case 1

The synchronous generator is described by a three-state model that includes the mechanical equations of motion and the governor. The power generated by the renewable resource of Bus 2 is modeled as an unknown-but-bounded static injection, i.e., following the notation in (2), $\dot{z} = 0$. The functions $g(x, y, u)$ and $h(x, y, v)$ are described in Appendix B1.

The procedure described in Section III is followed—we used MATLAB to implement the system models and also to implement the algorithms for reachability analysis. In this case, $u^*(t) = P_c = 0.6$ pu, and $v^*(t) = P_2 = 0.4$ pu are constant for $0 \le t \le \tau$, with $\tau = 20$ s, so the resulting linearized model described in (7) is time invariant. Following the notation in (7), in order to obtain x^* and y^* needed for computing the linearized model matrices, the steady-state solution of (27) and (28) is obtained by setting all the derivatives to zero and solving for all unknowns. Using the parameters in Table II, this results in $\omega_o = 120\pi$ rad/s, $P_{mo} = 0.6$ pu, $E_{1o} = 1.13$ pu, $V_{1o} = 1$ pu, $V_{2o} = 0.94$ pu, $V_{3o} = 0.94$ pu, $\theta_{1o} = -6.12°$, $\theta_{1o} - \theta_{3o} = 3.65°$, $\theta_{2o} - \theta_{3o} = 3.89°$.

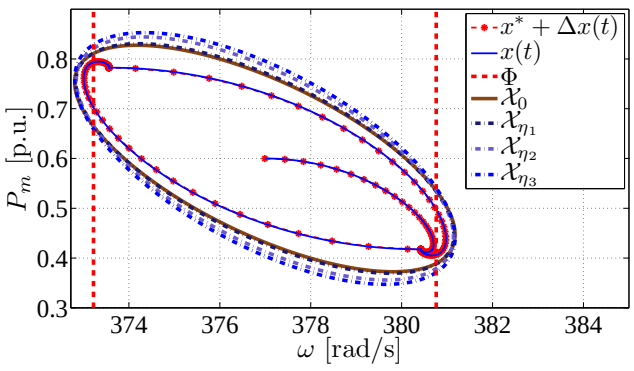

Fig. 7: Three-bus system reachability analysis results for wind power injection variability of ± 0.32 pu.

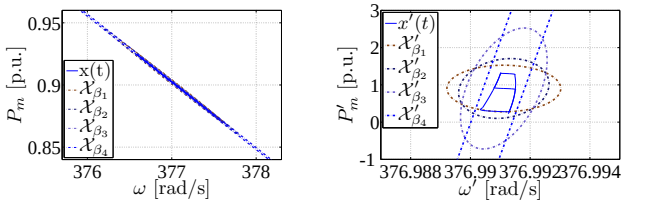

(a) Visualization in original P_m-ω coordinates.

(b) Visualization in rotated P_m-ω coordinates.

Fig. 8: Three-bus system reachability analysis results for wind variability of ± 1.6 m/s.

The unknown-but-bounded input disturbance is the power injection at Bus 2, which is denoted by v and assumed to vary between $\pm 80\%$ of its nominal value, i.e., $v \in [0.08, 0.72]$. In this case, since there is only one uncertain input, it follows that $Q = (0.8 \times 0.4)^2 = 0.1024$. The input uncertainty is then propagated through the system dynamics using (11), resulting in the reach set of the linearized system. Since the linearized matrix pair (A, B) is controllable, we choose the free parameter β in (11) by using (15).

Since there are only two dynamic states—ω and P_m—we can plot the linearized system state-bounding ellipsoids in the plane as shown in Fig. 7. The intersection of these ellipsoids is a tighter bound on the exact linearized system reach set. Also depicted Fig. 7 is a worst-case trajectory, which is created by switching between the two extrema of the input variation and roughly represents the reach set of the nonlinear system. In the same figure, a linearized system trajectory obtained from the same switching scheme is included, depicted with asterisks. We note the closeness to which the linearized system trajectory follows that of the nonlinear system and that the reach set of the nonlinear system is well approximated by the reach set obtained from the linearized system, i.e., $\mathcal{R} \approx \tilde{\mathcal{R}}$. The acceptable range for the state variable ω, which is given by the interval $[59.4, 60.6]$ Hz or $[373.03, 380.57]$ rad/s, is depicted in Fig. 7 by the vertical dashed traces. We note that, for the plotted trajectory, the excursions of ω are not entirely contained within the region defined by these two dashed traces, thus violating performance requirements. As expected, the violation is captured by the approximate reach set obtained from the linearized system.

B. Case 2

The synchronous generator is described by a five-state model, including the one-axis machine model, governor, and fast exciter/voltage regulator dynamics. In this case, the renewable-based resource considered is a Type-C WTG, which we describe by a first order dynamical model relating its power output, angular speed and wind speed. The inclusion of the WTG dynamics is an extension to a similar example considered in [5]. In this model, we use the augmented DAE description as in (2), where $g(x, y, u)$, $\alpha(z, w)$ and $\beta(z)$, and $h(x, y, v)$ are detailed in Appendices B2 and B3. In this case, it follows that $u^*(t) = [P_c,\ V_{ref}]^T = [0.903,\ 1.1083]^T$ and $w^*(t) = w_m = 8$ m/s, which are constant for $0 \le t \le \tau$, with $\tau = 20$ s. Hence, the resulting linearized model described in (7) is, again, time invariant. The unknown-but-bounded input is

wind speed, which we assume to be within $\pm 20\%$ of its nominal value, i.e., $w \in [6.4, 9.6]$ m/s and $Q = (8 \times 0.2)^2 = 2.56$.

Several ellipsoids are generated via (11), where the free parameter $\beta > 0$ is chosen randomly. In order to compare this case to the previous three-bus example, in Fig. 8(a) we plot the projections of the resulting ellipsoids onto the ω-P_m subspace by choosing the corresponding projector matrix as

$$H_{23} = \begin{bmatrix} 0 & 1 & 0 & 0 & 0 \\ 0 & 0 & 1 & 0 & 0 \end{bmatrix}.$$

The exact reach set of the linearized system is upper bounded by the intersection of these ellipsoids. In order to visualize the ellipsoids in Fig. 8(a) more clearly, we apply a rotation to both the ellipsoids and worst-case trajectory so the principle axes of one of the ellipsoids are in line with the Cartesian axes, as shown in Fig. 8(b). In this case, we note that the linearized system reach set upper bound does not cover the entire worst-case trajectory but is still a good approximation. Furthermore, by visual inspection of the ellipsoids (before rotation) in Fig. 8(a), we conclude that the excursion in ω do not violate performance requirements.

V. 39-Bus System Case Study

In this section, we analyze the performance of the 39-bus New England (NE) system for different renewable-based generation scenarios. In order to implement our analysis method, we modified the small-signal stability analysis capability of the MATLAB-based Power Systems Toolbox (PST) [31]. We also utilized MATLAB to implement the algorithms for reachability analysis discussed in Section III-B. The model of this system, which contains 10 synchronous units, is part of the PST suite and can be found in [31]. Units 1-9 are modeled by a 10^{th}-order ODE that includes mechanical equations of motion (2 states), damper/field windings (2 states), excitation system (3 states), and governor/turbine dynamics (3 states). Unit 10 model is fourth-order as it does not include the voltage regulator/exciter nor the governor/turbine, and has an artificially high inertia to mimic the slack bus behavior. The system real power generation is 61.93 pu.

Before proceeding in Section V-B with the system performance analysis for different renewable-based generation scenarios conducted, we present some analysis to verify the accuracy of our analysis procedure when utilized to study the New England system model. To this end, as in the three-bus example, we compare trajectories obtained by simulating the nonlinear system model with those obtained through the linearized model.

A. Accuracy of the Linearized Model

Consider a scenario in which the inertia of Unit 4 at Bus 33 is made artificially low to mimic a renewable-based power injection with fast dynamics, i.e., following the notation in (2), $\dot{z} = 0$. Then, the unknown-but-bounded input disturbance is the power injection from Unit 4, denoted as P_4, which has a nominal value of 6.32 pu.

We illustrate the accuracy of the linearized model by assuming several levels of variation in P_4 around the nominal

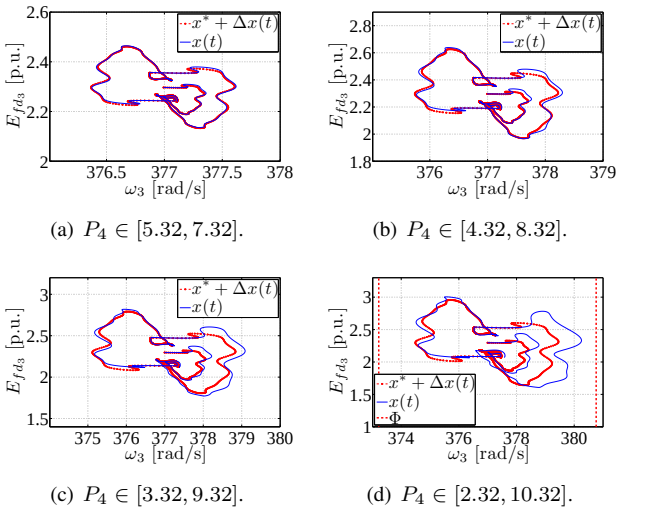

(a) $P_4 \in [5.32, 7.32]$. (b) $P_4 \in [4.32, 8.32]$.

(c) $P_4 \in [3.32, 9.32]$. (d) $P_4 \in [2.32, 10.32]$.

Fig. 9: Accuracy of linearized New England system model under wind power injection variability.

value. In particular, we consider scenarios with ± 1 pu, ± 2 pu, ± 3 pu, ± 4 pu variations around the nominal power injection value, i.e., variability levels of 15.8%, 31.6%, 47.4%, 63.3% respectively. For each of these variability levels, we generate a renewable-based power injection profile by switching (several times) between the two power injection extrema. The results are shown in Fig. 9, where we plot the projections of the resulting nonlinear and linearized system trajectories onto the subspace defined by the axes corresponding to E_{fd_3} and ω_3, which are the exciter field voltage and machine speed of Unit 3, respectively. We note that the linearized system trajectories indeed approximate the nonlinear trajectories closely for input variations of up to ± 2 pu (see Figs. 9(a) and 9(b)), which corresponds to more than 30% of the nominal power injection quantity. As expected, the linearized system trajectory begins to deviate from the nonlinear trajectory as the variability level in the power injection increases. In particular, as shown in Fig. 9(d), we observe significant deviations between the two trajectories for power injection variability of ± 4 pu, which corresponds to a variability level of almost 70%. It is also worth noting that, while the machine speed excursions are not as dramatic as those in the three-bus example, they are still significant; in particular, for 15.8%, 31.6%, 47.4% variability levels, the excursions of Unit 3 speed are 0.12 Hz, 0.19 Hz, 0.38 Hz, and 0.57 Hz respectively.

In subsequent analysis, we assume the linearized model approximates the nonlinear system sufficiently well and omit trajectories due to the difficulty in obtaining switching scenarios for worst-case trajectories given multiple input disturbances.

B. Case Studies

For the case studies presented in this section, we mimic integration of renewable-based generation by displacing certain synchronous generator with wind resources, and study system performance for several scenarios. The wind power plants are described by a first-order ODE following the models in [17] (also in [18, ch. 2]). We study the impact of wind variability on system dynamics for 20% and 30% penetration

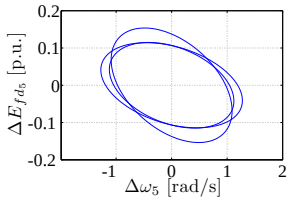

(a) Units 3, 6, and 7 displaced and participation of Units 1, 2, 4, 5, 8, 9.

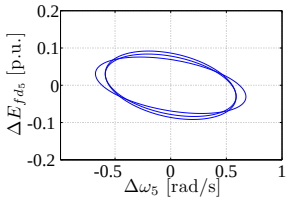

(b) Units 9 and 10 displaced and participation of Units 1-8.

Fig. 10: New England system with 30% renewable penetration, variability of ± 5 m/s, and governors in all non-displaced units.

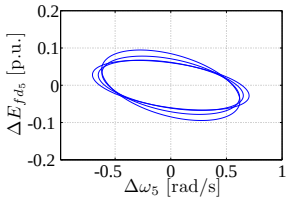

(a) Units 6 and 8 displaced, and participation of Units 1-5, 7, and 9.

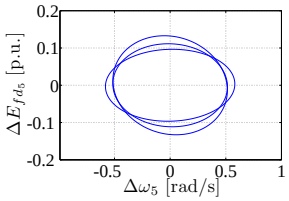

(b) Units 2 and 4 displaced, and participation of Units 1, 3, and 5-9.

Fig. 11: NE system with 20% renewable penetration, variability of ± 5 m/s, and governors in all non-displaced units.

with: i) different synchronous unit displacement scenarios, ii) two wind speed variability models: ± 3 m/s and ± 5 m/s, and iii) different units participating in governor response. As described in (12), in order to visualize reach set approximations, corresponding bounding ellipsoids are projected onto the subspace that contains the synchronous machine speed and exciter field voltage of a particular unit. In Figs. 10–13, in order to understand the effect of wind variability, attention must be paid to the intersection of ellipsoids, instead of the individual ones. Performance requirement limits are not displayed when the boundary of the ellipsoids is far away from these limits. The timeframe is $\tau = 60$ s for all studies.

1) Varying inertia, participation of all non-displaced units: We study the trade-offs between displaced amount of inertia, renewable penetration level, and participation in frequency control of non-displaced units.

Figure 10 depicts machine 5's speed and exciter field voltage deviations (denoted by $\Delta\omega_5$ and ΔE_{fd_5} respectively) for 30% wind penetration and two different scenarios: i) displacement of Units 3, 6, and 7 and participation in governor response of Units 1, 2, 4, 5, 8, and 9 (Fig. 10(a)), and ii) displacement of Units 9 and 10 and participation in governor response of Units 1-8 (Fig. 10(b)). Displacement of Units 9 and 10 represents a system inertia reduction of 53.45 s (the inertia constant of machine 10 is artificially large so as to mimic the slack bus behavior), whereas the displacement of Units 3, 6, and 7 represents a system inertia reduction of 6.12 s. We may reason that more deviations would be observed in Fig. 10(b), as this corresponds to the scenario with less total effective inertia; however, for machine speed, the opposite is observed. More insight into this paradox can be gained by considering the non-displaced unit governor participation. In Fig. 10(b), only one unit is effectively removed from primary frequency response, whereas, in Fig. 10(a), three units are removed.

We next compare system performance for the 20% penetration scenario, which results in less inertia reduction and more units participating in governor response with respect to the 30% penetration scenario of Figs. 10(a) and Fig. 10(b), of Fig. 11(a) with the scenario of Fig. 10(b). In this new scenario (Fig. 11(a)) Units 6 and 8 are displaced (with an effective inertia reduction of 5.91 s), and Units 1-5, 7, and 9 participating in governor response. In this case, the penetration of wind is reduced by 33% with respect to the one in Fig. 10(b), but there are still 16% fewer units participating in governor response than in the scenario of Fig. 10(b). In Fig. 11(a), it is observed that machine 5 speed deviations are approximately equal to those in Fig. 10(b).

While there may be trade-offs between inertia reduction, level of renewable penetration, and number of non-displaced synchronous generators that participate in primary frequency response, it seems that these trade-offs are clearly in favor of governor response participation from non-displaced units.

2) Fixed inertia, participation of different sets of units: With the amount of displaced inertia fixed, we study the difference in performance that results from different choices of non-displaced units participating in primary frequency control.

Figures 11(a) and 11(b) depict results for the cases in which the total displaced inertia is 5.91 s and 5.89 s, respectively. Also, both scenarios employ the same number of units for primary frequency response. Little difference in machine speed deviations for the two cases is observed. However, from this analysis, we cannot conclusively assert that the number of machines participating in governor response is the factor that causes the similarity between these scenarios, as shown next.

We compare the scenarios depicted in Fig. 12(a) and Fig. 12(b), where the effective inertia reduction is approximately equal and same as above, but the choice of units in partial governor participation is different. In Fig. 12(a), Units 1, 3, 5, and 7 are used, whereas in Fig. 12(b), Units 1, 3, 7, and 8 are used. The machine speed deviations shown in Fig. 12(a) are larger than those in Fig. 12(b), which indicates that, Unit 8 is more suited for primary frequency control than Unit 5 since Units 1, 3, and 7 are common to both scenarios. This finding is consistent with the droop characteristics of Unit 8 vs. Unit 5; more specifically, the steady-state gains for Unit 8 (165.6 pu), is much higher than that of Unit 5 (21.0 pu).

We now consider the scenario in which 30% renewable penetration is achieved by displacing Units 3, 6, and 7. In Fig. 13(a), machines 1, 2, and 4 partake in primary frequency control, and in Fig. 13(b), machines 2, 4, and 8. Even though both cases have three machines participating in governor response, the frequency deviations are larger in Fig. 13(a) than those in Fig. 13(b). This is again consistent with the droop characteristics of the governors/turbines on Units 1 and 8 (i.e., the steady-state gain for Unit 8 (165.6 pu) is greater than that of Unit 1 (110.1 pu)). Thus, it may be concluded that the governor on Unit 8 is more effective. Moreover, Fig. 13(a) shows that the choice of Units 1, 2, and 4 may be inadequate, as machine speed is outside the performance requirements region. The choice of Units 2, 4, and 8, on the other hand, yields acceptable results.

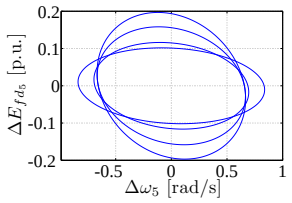

(a) Units 2 and 4 displaced, and participation of Units 1, 3, 5, and 7.

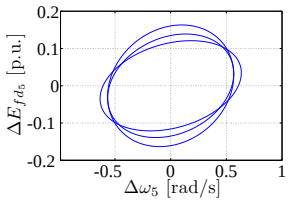

(b) Units 2 and 4 displaced, and participation of Units 1, 3, 7, and 8.

Fig. 12: NE system with 20% renewable penetration, and wind variability of ± 5 m/s.

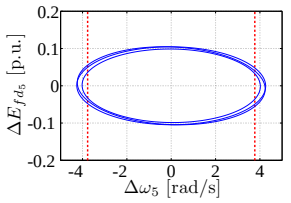

(a) Units 3, 6, and 7 displaced, and participation of Units 1, 2, and 4.

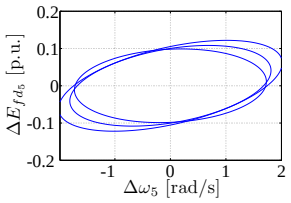

(b) Units 3, 6, and 7 displaced, and participation of Units 2, 4, and 8.

Fig. 13: NE system with 30% renewable penetration, and wind variability of ± 5 m/s.

VI. Concluding Remarks

This paper proposes a method to assess the impact of renewable resource variability on power system dynamics for time-scales involving electromechanical phenomena. With this method, we can determine whether certain variables of interest, such as synchronous generator speeds or system frequency, remain within acceptable ranges as the power system is subject to uncertainty in renewable-based generation, which may arise from inaccurate forecast of the primary source of energy (e.g., wind speed or solar insolation). We achieve this by describing the primary energy source variability in set-theoretic terms, and utilizing reachability analysis techniques for linear systems to obtain an approximation of the system reach set, the set that contains all possible system trajectories arising from all possible renewable-based power injection scenarios. We illustrate the application of this method to a three-bus system, where detailed derivations are presented. The method is also applied to the New England system model, from which several insightful observations are made.

Appendix

A. Derivation of Linearized Model

From (2), and under the assumptions stated in Section III-A, we can approximate $\Delta x(t)$, $\Delta y(t)$, and $\Delta z(t)$ by

$$\Delta\dot{x} = A_1(t)\Delta x + A_2(t)\Delta y, \tag{21}$$
$$\Delta\dot{z} = A_3(t)\Delta z + B(t)\Delta w, \tag{22}$$
$$\Delta v = C_1(t)\Delta z, \tag{23}$$
$$0 = C_2(t)\Delta x + C_3(t)\Delta y + C_4(t)\Delta v, \tag{24}$$

where,

$$A_1(t) = \frac{\partial g(x,y,u)}{\partial x}\Big|_{x^*,y^*,u^*}, \quad A_2(t) = \frac{\partial g(x,y,u)}{\partial y}\Big|_{x^*,y^*,u^*},$$
$$A_3(t) = \frac{\partial \alpha(z,w)}{\partial z}\Big|_{z^*,w^*}, \quad B(t) = \frac{\partial \alpha(z,w)}{\partial w}\Big|_{z^*,w^*},$$
$$C_1(t) = \frac{\partial \beta(z)}{\partial z}\Big|_{z^*}, \quad C_2(t) = \frac{\partial h(x,y,v)}{\partial x}\Big|_{x^*,y^*,v^*},$$
$$C_3(t) = \frac{\partial h(x,y,v)}{\partial y}\Big|_{x^*,y^*,v^*}, \quad C_4(t) = \frac{\partial h(x,y,v)}{\partial v}\Big|_{x^*,y^*,v^*},$$

with $v^* = \beta(z^*)$. In (24), as long as $C_3(t)$ is invertible, we can solve for Δy to obtain

$$\Delta y = -C_3^{-1}(t)\big[C_2(t)\Delta x + C_4(t)\Delta v\big]. \tag{25}$$

Then, substitute (25) into (21) and (22) to obtain a linear, time-varying ODE model:

$$\frac{d}{dt}\begin{bmatrix}\Delta x\\ \Delta z\end{bmatrix} = \begin{bmatrix}A_{11}(t) & A_{12}(t)\\ A_{21}(t) & A_{22}(t)\end{bmatrix}\begin{bmatrix}\Delta x\\ \Delta z\end{bmatrix} + \begin{bmatrix}B_1(t)\\ B_2(t)\end{bmatrix}\Delta w, \tag{26}$$

with $\Delta x(0) = \Delta z(0) = 0$, and where $A_{11}(t) = A_1(t) - A_2(t)C_3^{-1}(t)C_2(t)$, $A_{12}(t) = -A_2(t)C_3^{-1}(t)C_4(t)C_1(t)$, $A_{21}(t) = 0$, $A_{22}(t) = A_3(t)$, $B_1(t) = 0$, $B_2(t) = B(t)$.

B. Models in Three-Bus Example

1) Three-state differential-algebraic model: Let δ [rad] be the rotor electrical angular position, ω [rad/s] be the rotor electrical angular speed, P_m [pu] be the turbine mechanical power, and P_c [pu] be the unit power setting, which is assumed to be constant. Let V_i [pu], $i = 1,2,3$, denote the i^{th} bus voltage magnitude, and θ_i [rad], $i = 1,2,3$, denote the i^{th} bus voltage angle referenced to the synchronous machine angle δ. Following the notation in (2), define $x = [\delta,\ \omega,\ P_m]^T$, $y = [V_1,\ \theta_1,\ V_2,\ \theta_2,\ V_3,\ \theta_3]^T$, $u = P_c$. Then, the components of the vector function $g(x,y,u)$ in (2) are

$$\begin{aligned}\dot{\omega} =& \frac{1}{M}\big[-D(\omega-\omega_s) + P_m\\ &- \frac{EV_1}{X_m}\sin(-\theta_1)\big] =: g_1(x,y,u),\\ \dot{P}_m =& \frac{1}{T_{SV}}\left[-P_m + P_c - \frac{1}{R_D}\left(\frac{\omega}{\omega_s} - 1\right)\right] =: g_2(x,y,u),\end{aligned} \tag{27}$$

where ω_s [rad/s], D [s/rad], M [s^2/rad], E [pu], T_{SV} [s], and R_D [pu] are machine parameters [2]. Note that by using δ as a reference angle, the ODE governing its evolution is $\dot{\delta} = 0$ and is therefore omitted. The components of the vector function $h(x,y,v)$ in (2) are given by

$$\begin{aligned}0 =& v - Y_{23}V_2V_3\sin(\theta_2-\theta_3) =: h_1(x,y,v),\\ 0 =& Y_{23}V_2^2 - Y_{23}V_2V_3\cos(\theta_2-\theta_3) =: h_2(x,y,v),\\ 0 =& Y_{13}V_1V_3\sin(\theta_1-\theta_3)\\ &- Y_mEV_1\sin(-\theta_1) =: h_3(x,y,v),\\ 0 =& (Y_{13}+Y_m)V_1^2 - Y_{13}V_1V_3\cos(\theta_1-\theta_3)\\ &+ Y_mV_1^2 - Y_mEV_1\cos\theta_1 =: h_4(x,y,v)\\ 0 =& -P_3 - Y_{13}V_1V_3\sin(\theta_3-\theta_1)\\ &- Y_{23}V_2V_3\sin(\theta_3-\theta_2) =: h_5(x,y,v),\\ 0 =& -Q_3 - (Y_{13}+Y_{23})V_3^2 + Y_{13}V_1V_3\cos(\theta_3-\theta_1)\\ &+ Y_{23}V_2V_3\cos(\theta_3-\theta_2) =: h_6(x,y,v),\end{aligned} \tag{28}$$

where the $Y_{ik} = 1/X_{ik}$'s are the line admittances (see Fig. 6).

TABLE II: Parameter values for synchronous generator and network in three-bus system model example.

P_3	Q_3	Q_2	X_{13}	X_{23}	X_m	M [s^2/rad]	D [s/rad]	P_c	ω_s [rad/s]	T_{SV}	R_D	T_{d0}	X_d	X'_d	X_q	T_E	K_A
1	0.5	0	0.1	0.15	0.2	$\frac{1}{15\pi}$	0.04	0.6	120π	0.2	0.05	5.89	1.31	0.18	1.26	0.2	20

2) Five-state differential-algebraic model: Let E'_q [pu] be the scaled q-axis voltage, E_{fd} [pu] be the scaled field voltage, and V_{ref} be the exciter reference voltage setting. Further, let I_d and I_q [pu] be the stator currents. Following the notation in (2), define $x = [E'_q,\ \delta,\ \omega,\ P_m,\ E_{fd}]^T$, $y = [I_d,\ I_q, V_1,\ \theta_1,\ V_2,\ \theta_2,\ V_3,\ \theta_3]^T$, $u = [P_c,\ V_{ref}]^T$. Then, the components of the vector function $g(x, y, u)$ in the augmented DAE model of (2) are given by

$$\begin{aligned}
\dot{E}'_q =& \frac{1}{T_{d0}}\left[-E'_q - (X_d - X'_d)I_d + E_{fd}\right] =: g_1(x, y, u),\\
\dot{\omega} =& \frac{1}{M}\big[- D(\omega - \omega_s) + P_m - E'_q I_q\\
& - (X_q - X'_d)I_d I_q\big] =: g_2(x, y, u),\\
\dot{P}_m =& \frac{1}{T_{SV}}\left[-P_m + P_c - \frac{1}{R_D}\left(\frac{\omega}{\omega_s} - 1\right)\right] =: g_3(x, y, u),\\
\dot{E}_{fd} =& \frac{1}{T_E}\left[-E_{fd} + K_A(V_{ref} - V_t)\right] =: g_4(x, y, u),
\end{aligned} \tag{29}$$

where

$$\begin{aligned}
I_d &= \frac{1}{X'_d}\left[E'_q - V_1\cos(\theta_1 - \delta)\right],\\
I_q &= \frac{1}{X_q}\left[-V_1\sin(\theta_1 - \delta)\right],
\end{aligned}$$

with T_{d0}, X_d, X'_d, I_d, I_q, X_q, T_E, K_A and V_t being the model constant parameters [2].

The components of $h(x, y, v)$ are given by

$$\begin{aligned}
0 =& v - Y_{23}V_2V_3\sin(\theta_2 - \theta_3) =: h_1(x, y, v),\\
0 =& Y_{23}V_2^2 - Y_{23}V_2V_3\cos(\theta_2 - \theta_3) =: h_2(x, y, v),\\
0 =& I_dV_1\sin(\theta_1 - \delta) - I_qV_1\cos(\theta_1 - \delta)\\
& + Y_{13}V_1V_3\cos(\theta_3 - \theta_1) =: h_3(x, y, v),\\
0 =& - I_dV_1\cos(\theta_1 - \delta) - I_qV_1\sin(\theta_1 - \delta)\\
& + Y_{13}V_1^2 - Y_{13}V_1V_3\cos(\theta_1 - \theta_3) =: h_4(x, y, v)\\
0 =& - P_3 - Y_{13}V_1V_3\sin(\theta_3 - \theta_1)\\
& - Y_{23}V_2V_3\sin(\theta_3 - \theta_2) =: h_5(x, y, v),\\
0 =& - Q_3 - (Y_{13} + Y_{23})V_3^2 + Y_{13}V_1V_3\cos(\theta_3 - \theta_1)\\
& + Y_{23}V_2V_3\cos(\theta_3 - \theta_2) =: h_6(x, y, v),
\end{aligned} \tag{30}$$

3) First-order wind turbine generator model: Denote w_2 [m/s] as the wind speed at the location where the turbine is located, ω_t [rad/s] the wind turbine rotor speed, and P_2 [pu] the power injected in the network by the wind turbine. It is assumed that the turbine is operated in power factor mode with unit power factor, i.e., $Q_2 = 0$ (the model can be easily modified to account for operation in voltage control mode). Additionally, we assume that the WTG is operating between cut-in and rated speeds (constant pitch angle), and that stator and rotor dynamics, and active and reactive power controls are much faster than the mechanical motion.

Then, through singular-perturbation analysis [32], and neglecting stator losses, it can be shown that the WTG 10^{th}-order model in [16] (also in [18, pp. 14-20]) can be described by a first order dynamical model relating its power output, angular speed, and wind speed. Thus, following the notation in (2), define $w = w_2$, $z = \omega_t$, and $v = P_2$; the functions $\alpha(z, w)$ and $\beta(z)$ describing the WTG power output are

$$\begin{aligned}
\dot{z} &= \frac{\omega_s}{M_r}\left[BC_p(z, w)\frac{w^3}{z} - Cz^2\right] =: \alpha(z, w),\\
v &= cz^3 =: \beta(z),
\end{aligned} \tag{31}$$

where ω_s [rad/s] is the synchronous speed, $C_p(z, w)$ (dimensionless) is the power coefficient, M_r [s^2/rad] is the scaled inertia constant, and B [s^3/m^3] and C [s^3/rad^3] are constants related to turbine geometry and power settings, respectively.

Linearization of (31) yields

$$\begin{aligned}
\Delta\dot{z} =& a\Delta z + b\Delta w,\\
\Delta v =& c\Delta z,
\end{aligned}$$

where $a = -5.53 \cdot 10^{-2}$ pu, $b = 2.91$ pu, and $c = 9.37 \cdot 10^{-4}$ pu [18, p. 54].

REFERENCES

[1] B. Parsons *et al.*, "Grid impacts of wind power variability: Recent assessments from a variety of utilities in the united states," National Renewable Energy Laboratory, Tech. Report NREL/CP-500-39955, 2006.

[2] P. Sauer and M. Pai, *Power System Dynamics and Stability*. Upper Saddle River, NJ: Prentice-Hall, Inc., 1998.

[3] D. Gautam, V. Vittal, and T. Harbour, "Impact of increased penetration of dfig-based wind turbine generators on transient and small signal stability of power systems," *IEEE Trans. Power Syst.*, vol. 24, no. 3, pp. 1426–1434, Aug. 2009.

[4] J. Eto *et al.*, "Use of frequency response metrics to assess the planning and operating requirements for reliable integration of variable renewable generation," Lawrence Berkeley National Laboratory, Tech. Report LBNL-4142E, 2010.

[5] Y. Chen and A. Domínguez-García, "Assessing the impact of wind variability on power system small-signal reachability," *in Proc. of Hawaii International Conference on System Sciences*, January 2011.

[6] Z. Wang and F. Alvarado, "Interval arithmetic in power flow analysis," *IEEE Trans. Power Syst.*, vol. 7, no. 3, pp. 1341–1349, Aug. 1992.

[7] A. Saric and A. Stanković, "Model uncertainty in security assessment of power systems," *IEEE Trans. Power Syst.*, vol. 20, no. 3, pp. 1398–1407, Aug. 2005.

[8] ——, "An application of interval analysis and optimization to electric energy markets," *IEEE Trans. Power Syst.*, vol. 21, no. 2, pp. 515 – 523, May 2006.

[9] ——, "Applications of ellipsoidal approximations to polyhedral sets in power system optimization," *IEEE Trans. Power Syst.*, vol. 23, no. 3, pp. 956–965, Aug. 2008.

[10] I. Hiskens and M. Pai, "Trajectory sensitivity analysis of hybrid systems," *IEEE Trans. Circuits Syst. I: Fundam. Theory Appl.*, vol. 47, no. 2, pp. 204 –220, Feb. 2000.

[11] I. Hiskens and J. Alseddiqui, "Sensitivity, approximation, and uncertainty in power system dynamic simulation," *IEEE Trans. Power Syst.*, vol. 21, no. 4, pp. 1808 –1820, Nov. 2006.

[12] L. Jin *et al.*, "An application of reachable set analysis in power system transient stability assessment," in *Proc. of the IEEE Power Engineering Society General Meeting*, June 2005.

[13] L. Jin, R. Kumar, and N. Elia, "Reachability analysis based transient stability design in power systems," *International Journal of Electrical Power and Energy Systems*, vol. 32, no. 7, pp. 782–787, 2010.

[14] F. Schweppe, *Uncertain Dynamic Systems*. Englewood Cliffs, NJ: Prentice-Hall Inc., 1973.

[15] F. Milano, *Power System Modelling and Scripting*. London, UK: Springer, 2010.

[16] H. A. Pulgar-Painemal, "Reduced-order model of type-c wind turbine generators," *Electric Power Systems Research*, vol. 81, no. 4, pp. 840 – 845, 2011.

[17] ——, "Towards a wind farm reduced-order model," *Electric Power Systems Research*, vol. 81, no. 8, pp. 1688–1695, 2011.

[18] ——, "Wind farm model for power system stability analysis," Ph.D. dissertation, University of Illinois at Urbana-Champaign, 2010.

[19] D. L. King *et al.*, "Performance model for grid-connected photovoltaic inverters," Sandia National Laboratories, Technical Report SAND2007-5036, September 2007.

[20] M. Athans and P. Falb, *Optimal Control: An Introduction to the Theory and Its Applications*. McGraw-Hill Book Company, 1966.

[21] A. Kurzhanski and I. Vályi, *Ellipsoidal Calculus for Estimation and Control*. Boston, MA: Birkhauser, 1997.

[22] F. Chernousko, "What is ellipsoidal modelling and how to use it for control and state estimation," in *Whys and Hows in Uncertainty Modelling*. Vienna, Austria: Springer, 1999, pp. 127–188.

[23] A. Kurzhanski and P. Varaiya, "Ellipsoidal techniques for reachability analysis. Parts I & II," *Optimization Methods and Software*, vol. 17, pp. 177–206 and 207–237, Feb. 2000.

[24] M. Kendall, *A course in the Geometry of n Dimensions*. New York, NY: Hafner, 1961.

[25] S. Boyd and L. Vandenberghe, *Convex Optimization*. Cambridge, 2004.

[26] R. Horn and C. Johnson, *Topics in Matrix Analysis*. New York, NY: Cambridge University Press, 1991.

[27] M. Kvasnica, P. Grieder, M. Baotic, and M. Morari, "Multi-Parametric Toolbox (MPT)," in *HSCC (Hybrid Systems: Computation and Control)*, Mar. 2004, pp. 448–462. [Online]. Available: http://control.ee.ethz.ch/index.cgi?page=publications;action=details;id=53

[28] A. Girard, "Reachability of uncertain linear systems using zonotopes," in *HSCC*, 2005, pp. 291–305.

[29] A. Kurzhanskiy and P. Varaiya, "Ellipsoidal techniques for reachability analysis of discrete-time linear systems," *IEEE Transactions on Automatic Control*, vol. 52, no. 1, pp. 26 –38, Jan. 2007.

[30] A. A. Kurzhanskiy and P. Varaiya, "Ellipsoidal toolbox," EECS Department, University of California, Berkeley, Tech. Rep. UCB/EECS-2006-46, May 2006. [Online]. Available: http://code.google.com/p/ellipsoids

[31] Power system toolbox. [Online]. Available: http://www.eps.ee.kth.se/personal/vanfretti/pst

[32] P. Kokotović, H. Khalil, and J. O'Reilly, *Singular Perturbation Methods in Control: Analysis and Design*. London, UK: Academic Press Inc., 1986.